energies

MDPI

Article

Research on Natural Gas Hydrate Particle Size Prediction Model Based on DCSMHyK-PBM

Jianwei Han [1], Xiuhua Shan [1,*], Keping Zhai [2] and Shuang Jiang [3]

[1] Department of Petroleum Engineering, Hebei Petroleum University of Technology, Chengde 067000, China; hjwcy1104@163.com
[2] Department of Thermal Engineering, Hebei Petroleum University of Technology, Chengde 067000, China; kp_zhai0825@163.com
[3] Department of Mathematics and Physics, Hebei Petroleum University of Technology, Chengde 067000, China; 19133069266@163.com
* Correspondence: shxhus@163.com; Tel.: +86-15930093228

Abstract

Agglomeration of gas hydrate particles inside deepwater multiphase oil-and-gas flowlines can readily induce pipeline plugging, threatening the safe and efficient transportation of offshore energy resources. Accurate prediction of the dynamic evolution of hydrate particle size is crucial for assessing flow safety risks and formulating hydrate management strategies. The cohesive force in the CSMHyK model uses only subcooling as the input variable and lacks a temporal evolution mechanism, resulting in limited dynamic prediction accuracy. Addressing these limitations, this paper proposes a DCSMHyK-PBM coupling model. First, the Derjaguin microscopic liquid-bridge adhesion mechanism is introduced to replace the empirical subcooling-based cohesion formula, realizing the physical closure of inter-particle cohesion force through interfacial properties and particle radius. Second, the population balance model (PBM) with time-dependent partial differential equations is adopted to replace the original steady-state equilibrium algebraic particle-size formula, enabling dynamic output of particle size distribution and average agglomerate size over time. Finally, the model is designed to be compatible with an industrial transient multiphase flow framework through a time-stepping iteration logic. Validation against FBRM in situ measured chord length distribution data shows that the predicted CLD curves are consistent with experimental trends across six representative time points (four calibration and two independent validation), with an overall mean absolute relative deviation (MARD) of 8.68%, demonstrating that the improved model provides reasonable dynamic prediction of hydrate particle size evolution, contributing to safe and efficient offshore energy production and flow assurance in deepwater oil-and-gas transportation systems.

Keywords: natural gas hydrate; flow assurance; particle agglomeration; CSMHyK; PBM model; capillary liquid bridge force; FBRM; offshore energy production

Check for updates

Academic Editor: Krzysztof Skrzypkowski

Received: 20 September 2026
Revised: 18 October 2026
Accepted: 21 October 2026
Published: 2 November 2026

Copyright: © 2026 by the authors. Licensee MDPI, Basel, Switzerland. This article is an open access article distributed under the terms and conditions of the Creative Commons Attribution (CC BY) license.

1. Introduction

Driven by the accelerated global low-carbon energy transition and growing energy demand, deepwater oil-and-gas development continues to expand in scale, serving as a critical source of natural gas supply. The high-pressure and low-temperature environment of subsea flowlines can easily promote the formation of solid hydrate microcrystals from natural gas and free water. Particle agglomeration and deposition of hydrate microcrystals can lead to reduced flowline throughput, increased pressure drop, and even complete

blockage, posing significant threats to the safe operation of deepwater production systems and disrupting the reliable supply of offshore energy resources [1–6]. Therefore, accurate prediction of hydrate particle size evolution is of great importance for flow assurance risk assessment and hydrate management strategy formulation, supporting the safe and efficient transportation of natural gas as a clean energy source.

Numerical simulation studies on the agglomeration behavior of hydrate particles can be divided into three key development stages: the empirical fitting stage, the steady-state equilibrium algebraic-model stage, and the refined dynamic population-balance simulation stage.

Early research was constrained by multiphase flow testing equipment and numerical algorithms, establishing a linear exponential empirical correlation between average particle size with shear rate, subcooling, and water content, solely relying on experimental data of macroscopic viscosity and deposition amount [7–10]. Although these empirical formulas are simple in form, they lack physical mechanisms and have poor generalization ability across different operating conditions.

In 2002, Camargo [11] first proposed the theory of instantaneous force balance between agglomeration and breakage. This theory assumes that the system instantaneously reaches a dynamic equilibrium between agglomeration and breakage. By solving for the steady-state maximum agglomerate size based on the balance between the cohesive force and the fluid shear fragmentation force, and further deriving the average particle size through the fractal dimension, the CSMHyK (Colorado School of Mines Hydrate Kinetics) model was established [12–16]. The core breakthrough in this stage lies in establishing a quantitative correlation between "microscopic forces" and "macroscopic average particle size", breaking away from the limitations of purely empirical fitting. It has been adopted by multiple global oil-and-gas companies as a standard calculation module for multiphase flow simulation software.

Subsequent numerous scholars have conducted condition adaptability verification for CSMHyK. Boxall, Sinquin, et al. [17–20] conducted batch experiments targeting water-in-oil systems and gas-dominated systems, respectively, confirming that the model possesses certain predictive accuracy within the measured parameter range [21–25]. In recent years, in situ FBRM measurements in high-pressure hydrate slurry flow loops have further advanced the quantitative characterization of hydrate particle size distribution and anti-agglomerant performance under flow conditions [26]. However, the cohesive force closure of the CSMHyK model adopts the Dieker formula, which uses subcooling as the sole input variable without considering microscopic interfacial effects such as capillary liquid bridge forces and van der Waals forces, making it essentially an empirical fitting formula.

Early PBM hydrate research often adopted simplified agglomeration efficiency and kernel, without coupling microscopic interfacial adhesion mechanisms. The probability of particle adhesion after collision relied on constant calibration, resulting in insufficient physical completeness. In recent years, Balakin et al. [27–29] pioneered the application of the population balance model (PBM) to hydrate particle agglomeration simulation, establishing a CFD-PBM coupling framework that considers nucleation, growth, agglomeration, and breakage processes. Subsequent studies further expanded the application scenarios of PBM in hydrate flow assurance.

Recent studies have further revealed that multiscale vortex structures in turbulent flows significantly influence particle collision and agglomeration dynamics. Cylindrical disturbances and flow passage transitions can generate localized vortices that enhance particle transport, collision frequency, and aggregation efficiency [30,31]. Numerical investigations of particle-laden vortex flows have demonstrated that counter-rotating vortex pairs can induce localized particle clustering and periodic leakage, fundamentally altering the

collision statistics compared with uniform-shear assumptions [32]. In hydrate-specific systems, diameter transitions in flow loops have been shown to induce vortices at the reducer shoulders, which promote hydrate particle deposition and accumulation, making such geometries preferential blockage locations [33]. These findings indicate that the conventional uniform-shear collision kernel adopted in most PBM hydrate models may not fully capture the vortex-enhanced collision and agglomeration mechanisms present in complex pipeline geometries.

Existing research still has significant gaps. The vast majority of improvement schemes only independently correct the adhesion force formula or independently introduce PBM dynamic evolution, without deeply coupling the Derjaguin microscopic liquid bridge adhesion mechanism with industrial-grade transient multiphase flow frameworks [34,35]. There is a lack of a dynamic prediction model that simultaneously satisfies physical mechanism completeness and industrial-grade computational efficiency.

Addressing the inherent limitations of the traditional CSMHyK model, namely the empirical nature of its cohesion force formula, lack of temporal evolution, and output of a single equilibrium particle size, this paper retains the established hydrate shell growth kinetics and multiphase rheological core of CSMHyK, and proposes a DCSMHyK-PBM coupling model from two dimensions: (1) introducing the Derjaguin capillary liquid bridge adhesion mechanism to achieve physically based closure of inter-particle cohesion force; (2) adopting the population balance model (PBM) to replace the steady-state algebraic particle size formula, realizing dynamic output of particle size distribution over time. The model is validated against FBRM experimental data, providing a new tool for hydrate flow assurance risk assessment.

2. Hydrate Formation Mechanism

2.1. Formation Process

Hydrate formation primarily involves five processes: nucleation, growth, agglomeration, sedimentation, and blockage, as illustrated in Figure 1. In oil-dominated systems, oil and water come into contact under the effects of wall shear and flow shear, forming numerous mutually independent small water droplets. Under high-pressure and low-temperature conditions, guest molecules (natural gas components) dissolve into the water droplets and react with water molecules to form hydrate crystals. As hydrate formation proceeds, the water droplets are gradually converted into hydrate particles, and these particles collide and agglomerate under the action of flow field shear, Brownian motion, and differential settling, eventually forming large agglomerates that may deposit at the bottom of the flowline and cause blockage.

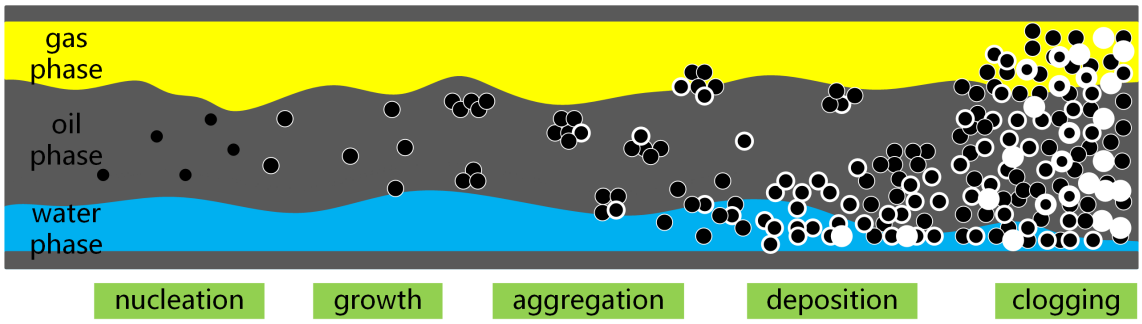


Figure 1. Hydrate formation within oil-dominated multiphase flowlines.

2.2. Nucleation Mechanism

The hydrate nucleation mechanisms mainly include the cluster nucleation mechanism, the local structure nucleation mechanism, and the interface nucleation mechanism [36–38]. The cluster nucleation mechanism posits that the internal polygonal structures of water molecules and water molecule clusters continuously rearrange and combine under the driving force of subcooling, gradually forming cage-like cluster structures that can encapsulate guest molecules. Guest molecules are surrounded by rearranged water molecules to form cage-like cluster structures with guest molecules at the core and water molecules in the periphery, namely the crystal-lattice structure. Driven by subcooling, multiple lattices grow outward continuously and finally form hydrate crystal nuclei.

In accordance with the local-structure nucleation mechanism, water molecules do not undergo cleavage and reconstruction. Instead, guest molecules are directly incorporated into intrinsic polyhedral structures within bulk liquid water to form cage-like clusters. These clusters correspond to crystal-lattice structures and can grow into stable hydrate nuclei when their size exceeds the critical nucleation radius.

For the interfacial nucleation mechanism, hydrate nuclei form near the gas–liquid interface. Water molecules attract and trap guest molecules to construct lattice-type cage structures, which further grow into hydrate crystal nuclei. This mechanism is particularly important in gas-dominated systems where the gas-liquid interfacial area is large.

The three nucleation mechanisms are illustrated in Figures 2–4.

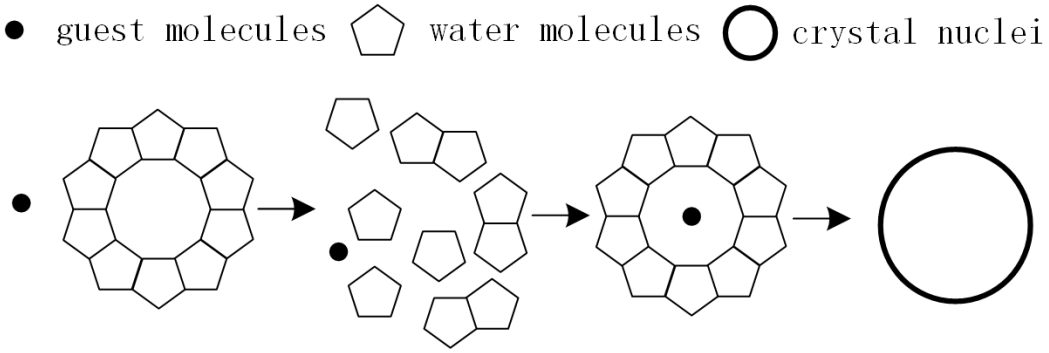


Figure 2. Cluster nucleation mechanism.

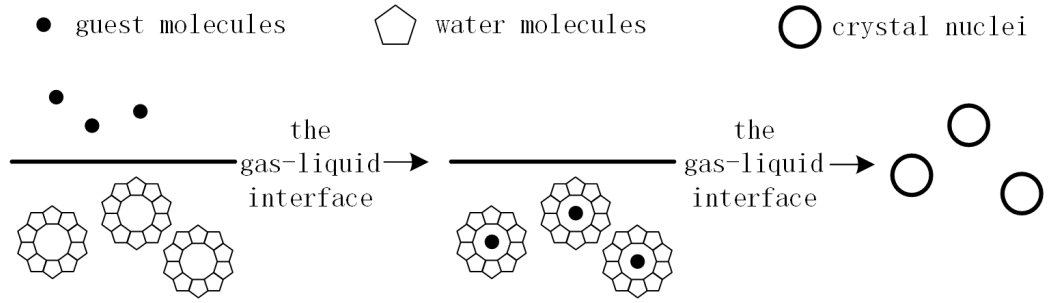


Figure 3. Local structure nucleation mechanism.

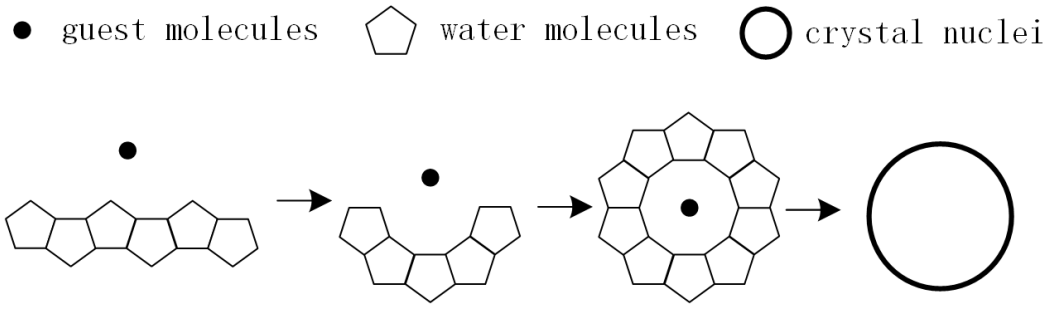


Figure 4. Interface nucleation mechanism.

2.3. Growth Mechanism

Hydrate is formed around the outer surface of water droplets in contact with guest molecules [39,40]. A closed hydrate shell is generated when hydrate particles expand and grow to cover the entire outer surface of the water droplets. The hydrate shell encapsulates the outer surface of the water droplets, isolating the internal unreacted water from the guest molecules. Subsequent hydrate growth is controlled by the diffusion of guest molecules through the hydrate shell and the intrinsic reaction kinetics at the shell–water interface. The Zerpa growth model describes this process by assuming that hydrate first forms a shell on the droplet surface, and then gas penetrates the shell to react with the internal water, causing the hydrate layer to thicken inward until the entire droplet is converted.

The growth process of hydrate particles is illustrated in Figure 5.

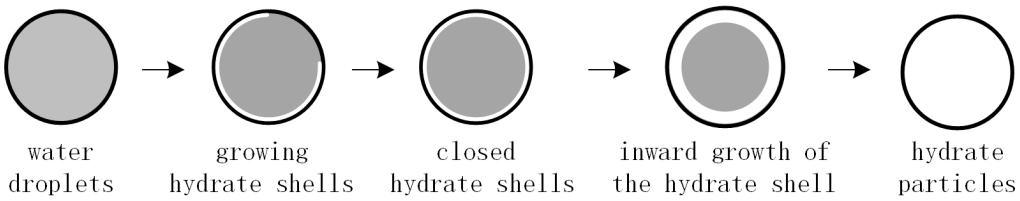


Figure 5. Growth process of hydrate particles.

2.4. Agglomeration Mechanisms

In hydrate suspensions, growing hydrate particles and unreacted water droplets coexist [41,42]. Through contact-induced migration, a portion of water droplets converts into hydrates, while others come into contact with hydrate particles and wet their outer surfaces. Driven by flow-field disturbances, Brownian motion, and differential settling, particles collide with each other. When the inter-particle cohesive force (primarily capillary liquid bridge force) exceeds the fluid shear fragmentation force, the colliding particles adhere stably and form agglomerates. The agglomerates exhibit fractal characteristics, and their effective volume fraction is significantly larger than the solid volume fraction due to the liquid trapped within the agglomerate structure.

2.5. Deposition Mechanism

The primary mechanisms of hydrate deposition include flowline impaction, pipe wall film growth, and pipe wall adhesion [43–48]. The flowline impaction mechanism divides deposition into three stages: uniform suspension, non-uniform suspension, and deposition impaction. During the initial formation of hydrates, particles are uniformly distributed in the flow cross-section. As particle size increases due to agglomeration, the gravitational settling velocity exceeds the turbulent dispersion capacity, causing particles to migrate toward the bottom of the flowline and form a non-uniform concentration distribution. Large agglomerates eventually impact and deposit on the pipe wall, forming a deposition layer.

Pipe wall film growth occurs when a continuous water film exists on the pipe wall. Hydrates form directly on the wall surface, and the hydrate film grows inward, reducing the effective flow area. Pipe wall adhesion involves the adhesion of hydrate particles to the wall surface under the action of van der Waals forces and capillary forces, which is particularly significant when the wall surface is wetted by water.

2.6. Blockage Mechanism

The growth, agglomeration, and deposition of hydrates all form the fundamental processes for flowline blockage [49–51]. When hydrate agglomerates exist in large quantities, with some hydrates depositing at the bottom of the flowline and the remaining hydrates filling the flowline's cross-section, a flowline blockage occurs. The blockage can be classified into two types: (1) deposition-type blockage, where hydrates gradually deposit on the pipe wall until the flow cross-section is completely sealed; (2) agglomeration-type blockage, where large hydrate agglomerates form a plug that moves with the flow and eventually gets stuck at a restriction or elbow. Both types can cause severe production interruption and safety hazards.

3. Model Establishment and Improvement

3.1. CSMHyK Model

3.1.1. Establishment of the CSMHyK Model

The Colorado School of Mines developed the CSMHyK model using a rheological approach to describe the behavioral changes in hydrate particles [13,14]. The CSMHyK model was applied in multiphase flow simulation, where the cohesive force between hydrate particles was obtained through empirical fitting. The rheological core of the model is based on the Richardson-type relative viscosity equation and the effective volume fraction concept for fractal agglomerates.

The relative viscosity of the hydrate suspension is given by the Richardson-type equation:

$$\mu_r = \frac{1-\phi_e}{\left[1-(\phi_e/\phi_{\max})\right]^2}, \tag{1}$$

where μ_r is the relative viscosity of the suspension; ϕ_e is the effective volume fraction of hydrate agglomerates; $\phi_{\max}$ is the maximum packing volume fraction. The relative viscosity is defined as the ratio of the apparent viscosity to the oil phase viscosity:

$$\mu_r = \mu_a/\mu_o, \tag{2}$$

where μ_a is the apparent viscosity of the suspension, Pa·s; μ_o is the viscosity of the oil phase, Pa·s.

The effective volume fraction of hydrate agglomerates accounts for the liquid trapped within the fractal agglomerate structure:

$$\phi_e = \phi_{hyd}\left(\frac{d_a}{d_0}\right)^{3-f}, \tag{3}$$

where ϕ_{hyd} is the volume fraction of hydrate particles; d_a is the average diameter of hydrate agglomerate particles, μm; d_0 is the diameter of initial hydrate particles, μm; f is the fractal dimension of hydrate agglomerate particles. According to the research by Hoffmann [52], a value of 0.57 is commonly used for $\phi_{\max}$. Sinquin [20] conducted relevant research on hydrate particles, and the recommended value of f ranges from 1.8 to 2.5.

Zerpa established a hydrate growth model, proposing that hydrates first form a shell on the surface of water droplets [17–19]. Under external driving forces, gas penetrates the shell to contact the water droplet internally, causing the hydrate to grow inward and eventually

form a complete hydrate particle. The initial hydrate particle size is determined by the Weber number criterion. When the Weber number satisfies the condition in Equation (6), the initial particle size is calculated by Equation (4):

$$d_0 = 0.063\, d\, We^{-0.6}, \tag{4}$$

where d is the water droplet diameter, m; We is the Weber number. The Weber number is defined as

$$We = \frac{\rho_o u^2 d}{\sigma}, \tag{5}$$

where ρ_o is the oil phase density, kg/m^3; u is the average flow velocity, m/s; σ is the oil–water interfacial tension, N/m. The criterion for selecting the initial particle size formula is

$$We < 0.0674\, Re^{1.25}, \tag{6}$$

where Re denotes the Reynolds number. When Equation (6) is not satisfied, the initial particle size is calculated using the Reynolds number correlation:

$$d_0 = 0.016\, d\, Re^{0.5}\, We^{-0.6}. \tag{7}$$

The maximum size of hydrate agglomerates is derived from the balance between the cohesive force and the fluid shear force, based on the Muhle model [53], as shown in Equation (8):

$$d_{a,\max} = \left[\frac{F_a\, d_0^{2-f}}{\mu_o\, \gamma}\right]^{\frac{1}{4-f}}, \tag{8}$$

where $d_{a,\max}$ is the maximum size of hydrate agglomerate particles, μm; F_a is the cohesive force between hydrate particles, N; γ is the shear rate, 1/s.

The average size of hydrate agglomerates is obtained by solving the implicit relationship given in Equation (9):

$$\left(\frac{d_a}{d_{a,\max}}\right)^{4-f} - \frac{F_a\left[1-\left(\phi_{hyd}/\phi_{\max}\right)\left(d_a/d_{a,\max}\right)^{3-f}\right]^2}{d_{a,\max}^2\, \mu_o\, \gamma\left[1-\phi_{hyd}\left(d_a/d_{a,\max}\right)^{3-f}\right]} = 0. \tag{9}$$

The cohesive force F_a between hydrate particles is calculated using the Dieker formula:

$$F_a = \frac{d_0}{2}[0.0017(7.7-\Delta T)+0.0007], \tag{10}$$

where ΔT denotes the system subcooling relative to the hydrate equilibrium curve, K.

3.1.2. CSMHyK Model Deficiencies

The cohesive force closure of the CSMHyK model adopts subcooling as its sole input variable, while neglecting microscopic interfacial effects including capillary liquid bridge forces and van der Waals forces. This closure is therefore an empirical fitting formula. Equations (8) and (9) represent steady-state equilibrium algebraic solutions that assume the system instantaneously reaches force balance, without considering the temporal evolution of particle size distribution. Consequently, the model can only output a single equilibrium average particle size and cannot describe the dynamic evolution process of particle size distribution over time, limiting its application in transient flow assurance risk assessment.

3.2. Establishment of the DCSMHyK-PBM Model

CSMHyK can be coupled with transient multiphase flow simulators to achieve multiphase flow simulation of hydrates, but the steady-state particle size solving module constrains its dynamic prediction capability. It introduces a population balance model (PBM) governed by time-dependent partial differential equations to replace the original steady-state algebraic particle size formula. Meanwhile, the Derjaguin microscopic liquid bridge adhesion mechanism is introduced to replace the empirical subcooling-based cohesion formula, achieving physically based closure of the inter-particle cohesion force.

3.2.1. DCSMHyK Model

Inter-particle cohesion is a core parameter controlling the agglomeration behavior of hydrates, directly influencing particle size and settling characteristics. Addressing the deficiencies in the original cohesion formula, hydrate particles are treated as equivalent spheres (force analysis is shown in Figure 6). Based on the Derjaguin approximation [54,55], the cohesive force between two spherical particles connected by a liquid bridge is derived from the interaction energy per unit area.

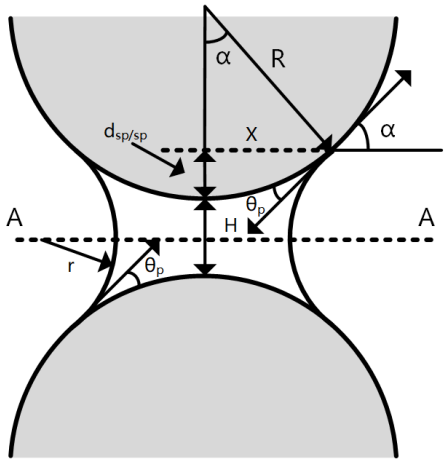


Figure 6. Force analysis between hydrate particles connected by a capillary liquid bridge.

The Derjaguin adhesion force between two spherical particles separated by a distance H is given by

$$F_a(H) = k\,R\,U(H), \tag{11}$$

where k is the interaction coefficient between particles, taking a value of 2π in the standard Derjaguin approximation [54]; R is the effective radius (R_{eff}) of two contacting hydrate particles, defined by $1/R = 1/R_1 + 1/R_2$, where R_1 and R_2 are the radii of the two contacting particles; for equal-sized particles $R = R_{\text{particle}}/2$, m; $U(H)$ is the interaction energy per unit area between two hydrate particles at separation distance H, J/m^2.

When two hydrate particles are connected by a thin liquid bridge, the interaction energy per unit area is determined by the capillary force:

$$U = -2\sigma\cos\theta, \tag{12}$$

where the product $\sigma\cos\theta$ is treated as a single combined interfacial parameter, with σ [N/m] denoting the interfacial tension and θ [°] the contact angle between the hydrate and liquid phases. In the present model, $\sigma\cos\theta$ is calibrated against the experimental FBRM chord length distribution data, rather than specifying σ and θ independently.

By substituting Equation (12) into Equation (11) and setting $H = 0$ (initial contact), the physically based cohesive force formula is obtained:

$$F_a(H=0) = -4\pi\sigma R_{\text{eff}}\cos\theta, \tag{13}$$

which replaces the empirical Dieker formula (Equation (10)) and realizes the closure of inter-particle cohesion force through the combined interfacial parameter $\sigma \cos\theta$ and the effective particle radius. It should be noted that the negative sign in Equations (12) and (13) indicates the attractive nature of the capillary force. For hydrate particles in oil-dominated systems, the contact angle θ is typically greater than 90° (hydrophobic surface), such that $\cos\theta < 0$ and the calculated adhesion force F_a is positive, representing an attractive inter-particle force. It should be clarified that R in Equations (11) and (13) denotes the effective radius R_{eff} of the two contacting particles, not the radius of an individual particle.

3.2.2. DCSMHyK-PBM Model

The population balance model (PBM) is adopted to replace the Camargo-Palermo steady-state particle size formula. The PBM control equation inherently includes time derivatives, which can fully describe the dynamic changes in particle number density and size distribution over time and flow fields.

(1) PBM Control Equation

Let $n(d,t)$ denote the number density of hydrate particles of particle size d at time t. The population balance equation for the coupled flow convection term under one-dimensional pipe transport is shown in Equation (14):

$$\frac{\partial n(d,t)}{\partial t} + u\frac{\partial n(d,t)}{\partial x} = B_a(d,t) - D_a(d,t) + B_b(d,t) - D_b(d,t) + B_{nuc}(d,t), \tag{14}$$

where the right-hand side denotes the source term for the temporal evolution of particle number density; u is the axial velocity of the hydrate slurry, m/s; x is the axial position of the pipe, m; B_a is the source term for particles of size d being generated from the collision and agglomeration of smaller particles; D_a denotes the sink term for particles of size d disappearing due to agglomeration with other particles; B_b and D_b are the source and sink terms for particle breakage, respectively; B_{nuc} is the hydrate nucleation/growth source term, representing the rate at which newly formed primary hydrate particles enter the size distribution.

(1a) Hydrate Nucleation Source Term

The hydrate nucleation source term accounts for the continuous generation of primary hydrate particles by the CSMHyK shell-growth kinetics. Newly formed hydrate particles enter the size distribution at the initial particle diameter $d_0(t)$:

$$B_{nuc}(d,t) = \dot{N}_{new}(t)\,\delta(d - d_0(t)), \tag{15}$$

where $\delta(\cdot)$ is the Dirac delta function, and $\dot{N}_{new}(t)$ is the number generation rate of primary hydrate particles per unit volume, determined by the hydrate volume fraction change rate computed from CSMHyK:

$$\dot{N}_{new}(t) = \frac{d\phi_{hyd}/dt}{\frac{\pi}{6}d_0(t)^3}, \tag{16}$$

where $d\phi_{hyd}/dt$ is the time derivative of the hydrate volume fraction provided by the CSMHyK module, and $\frac{\pi}{6}d_0^3$ is the volume of a single primary hydrate particle.

This formulation ensures conservative coupling between the CSMHyK hydrate formation kinetics and the PBM: the total hydrate volume is governed by the CSMHyK module (which retains the mature shell-growth kinetic equations), while the PBM distributes the newly formed hydrate mass into the particle size domain and resolves the subsequent agglomeration and breakage dynamics. The hydrate volume fraction computed from the PBM (by integrating $\frac{\pi}{6}d^3 n(d,t)$ over all sizes) is therefore consistent with the ϕ_{hyd} predicted by CSMHyK, avoiding double-counting or inconsistency.

It should be noted that the particle growth process (shell thickening) is accounted for by the CSMHyK module through the initial particle size d_0, which represents the hydrate particle size after complete shell formation. Once the hydrate shell is formed, the particle outer diameter remains approximately constant, and subsequent size changes are dominated by agglomeration and breakage, which are explicitly resolved by the PBM.

(2) Coalescence Kernel

Whether particles can stably adhere after collision depends on the relative magnitude of the bonding force and the flow field shear breakup force. The agglomeration efficiency is calculated by the ratio of the adhesion force to the shear force, as shown in Equation (17):

$$\alpha_a = \min\left(\frac{F_a}{F_s}, 1\right) = \min\left(\frac{F_a}{6\pi\mu_o\gamma d_p^2}, 1\right), \tag{17}$$

where F_s represents the shear force exerted by fluid on the particle, N; α_a is the agglomeration efficiency; and d_p is the hydrate particle diameter, m. The shear force is proportional to the square of the particle diameter, ensuring dimensional consistency (μ_o [kg/(m·s)] × γ [1/s] × d_p^2 [m^2] = N). The agglomeration efficiency is capped at unity: when $F_a/F_s > 1$, the cohesive force sufficiently exceeds the shear force such that all colliding particles adhere, giving $\alpha_a = 1$.

The collision frequency function between two particles under a shear flow field is shown in Equation (18):

$$\beta(d_i, d_j) = \frac{4}{3}\gamma\left(\frac{d_i}{2} + \frac{d_j}{2}\right)^3, \tag{18}$$

where d_i and d_j represent the diameters of two hydrate particles, m; $d_i/2$ and $d_j/2$ are the corresponding particle radii; β is the collision frequency between two hydrate particles. This formulation is consistent with the standard shear-induced collision kernel, which is expressed in terms of particle radii.

Combining the collision frequency and the agglomeration efficiency, the agglomeration generation and disappearance terms are obtained as shown in Equations (19) and (20). For the agglomeration birth term, volume conservation is enforced: when two particles of diameters d' and d'' agglomerate, the resulting particle diameter d satisfies $d^3 = d'^3 + d''^3$, i.e., $d'' = (d^3 - d'^3)^{1/3}$. A variable substitution from d'' to d is applied, introducing the Jacobian factor $d^2/(d^3 - d'^3)^{2/3}$:

$$\begin{aligned} B_a(d,t) = \frac{1}{2}\int_0^d \beta\left(d',\,(d^3-d'^3)^{1/3}\right)\alpha_a\left(d',\,(d^3-d'^3)^{1/3}\right) \\ \cdot\, n(d',t)\, n\left((d^3-d'^3)^{1/3},t\right)\frac{d^2}{(d^3-d'^3)^{2/3}}\,dd', \end{aligned} \tag{19}$$

$$D_a(d,t) = n(d,t)\int_0^\infty \beta(d,d')\,\alpha_a(d,d')\,n(d',t)\,dd'. \tag{20}$$

(3) Breakage Kernel

The dissociation rate of hydrate agglomerates under fluid shear is proportional to the shear rate and particle size, as shown in Equation (21):

$$S(d) = k_b\,\gamma\,d, \tag{21}$$

where S represents the breakage (dissociation) rate of hydrate agglomerates, with dimension of 1/s, and k_b is the breakage rate coefficient with dimension of 1/m, accounting for the probability of agglomerate fragmentation per unit shear and per unit particle size. The value of k_b is determined through calibration against experimental FBRM chord length distribution data.

The uniform breakup hypothesis is adopted for the breakup distribution function. By combining the breakup source and sink terms, Equations (22) and (23) are obtained:

$$B_b(d,t) = \int_d^\infty S(d')\, b(d|d')\, n(d',t)\, dd', \tag{22}$$

$$D_b(d,t) = S(d)\, n(d,t), \tag{23}$$

where $b(d|d')$ represents the probability distribution function of daughter particles d generated from the fragmentation of parent particles d'.

(4) Time-Varying Solution for Average Agglomerate Size

By integrating the particle number density distribution at an arbitrary moment t, the average agglomerate size at that moment is obtained, achieving dynamic output of particle size over time, as shown in Equation (24):

$$d_A(t) = \frac{\int_0^\infty d \cdot n(d,t)\, dd}{\int_0^\infty n(d,t)\, dd}. \tag{24}$$

(5) Initial Conditions and Time-Step Solution Logic for Transient Multiphase Flow

At the initial moment of the simulation, only primary hydrate particles derived from dispersed water droplets exist within the system. Particle collision and agglomeration have not yet occurred, and there are no large-sized agglomerates. The number density distribution of particles is given by

$$n(d,0) = \begin{cases} n_0, & d = d_0 \\ 0, & d \neq d_0 \end{cases} \tag{25}$$

where n_0 is the initial number concentration of primary hydrate particles, m^{-3}, obtained by integrating the hydrate-formation kinetics term, and d_0 is the primary initial hydrate particle size, calculated by Equations (4)–(7).

The entire coupled system is designed to follow the transient time-stepping framework of industrial multiphase flow simulation. While fully preserving the original hydrate-formation and multiphase-flow heat and mass transfer modules of CSMHyK, it only replaces the original algebraic solving procedure for steady-state equilibrium particle size with the PBM dynamic evolution module. The time-stepping iteration logic is as follows:

1. **Transient flow-field update**: The multiphase flow field is advanced by one time step Δt via the momentum, energy, and mass conservation equations for the oil, gas, and water phases, outputting time-varying field parameters: mixture velocity u, pipe shear rate γ, system temperature T, hydrate subcooling ΔT, and volume fraction ϕ_{hyd}.
2. **Hydrate formation kinetics solution**: Invoke the native shell-growth kinetic equation of CSMHyK. The amount of newly formed hydrate within the current time step is calculated based on the current subcooling ΔT, and the global hydrate volume fraction ϕ_{hyd} and its time derivative $d\phi_{hyd}/dt$ are updated accordingly. Meanwhile, the native particle initial size d_0 is updated using Equations (4)–(7). The hydrate formation rate $d\phi_{hyd}/dt$ serves as the driving input for the PBM nucleation source term.
3. **Instantaneous adhesion force calculation**: Substitute the calibrated combined interfacial parameter $\sigma \cos\theta$ and effective radius R of the contacting particle pair into Equation (13) to calculate the instantaneous inter-particle adhesion force F_a; this parameter reflects the magnitude of the microscopic force at the current moment and serves as the input to the agglomeration efficiency.

4. **Discrete solution of the population balance equation (PBE)**: Substituting F_a and γ into the agglomeration and breakage kernel functions, and computing the nucleation source term B_{nuc} from $d\phi_{hyd}/dt$ and d_0 according to Equations (15) and (16), the PBE partial differential control equation is discretized using the finite difference/moment method. In the numerical implementation, the Dirac delta source term is realized by directly adding the newly generated particle number ($\dot{N}_{new} \cdot \Delta t$) to the size bin corresponding to d_0. Combined with the particle distribution $n(d, t)$ at time t, the full particle size distribution $n(d, t + \Delta t)$ at the next moment is solved.
5. **Time-varying average agglomerate size integral output**: Integrate the particle number density distribution at time $t + \Delta t$ according to Equation (24) to obtain the average agglomerate size at the current step.
6. **Slurry rheological parameter update**: Substitute the time-varying particle size $d_A(t + \Delta t)$ into Equation (3) to update the effective volume fraction ϕ_e, and then substitute into the rheological equations (Equations (1) and (2)) to obtain the time-varying apparent viscosity μ_a of the suspension.
7. **Iteration**: Assign $n(d, t + \Delta t)$ to the initial particle-size distribution for the next cycle, return to step 1, and continue advancing the time step until the simulation hits the termination time or the pipe outlet cross-section.

Numerical Implementation Details

The population balance equation is discretized and solved using the following numerical settings:

- **Size grid**: The particle diameter range is discretized into $N = 64$ logarithmically uniform bins spanning from $d_{\min} = 0.5$ μm to $d_{\max} = 1000$ μm. The logarithmic grid provides higher resolution in the small-particle range where the primary particle peak occurs, while covering the full range of agglomerate sizes observed in the experiments.
- **Initial particle size distribution**: The initial PSD is represented by a lognormal distribution centered on the primary hydrate particle diameter D_p (4 μm for the Lyre loop, 7 μm for the Archimede loop, as reported in the reference experimental study), with a calibrated distribution width.
- **Time integration**: The resulting system of ordinary differential equations (ODEs) for the discretized number densities is integrated using the LSODA solver (Livermore Solver for Ordinary Differential Equations), with relative tolerance rtol = 10^{-4} and absolute tolerance atol = 10^{-10}. The LSODA solver automatically switches between non-stiff (Adams) and stiff (BDF) methods, which is well-suited for the potentially stiff agglomeration–breakage dynamics.
- **Boundary conditions**: Zero-flux boundary conditions are applied at both $d_{\min}$ and $d_{\max}$, meaning no particles enter or leave the computational domain through the size boundaries. The upper boundary $d_{\max} = 1000$ μm is sufficiently large that the particle number density remains negligible at this boundary for all simulated conditions.
- **Breakage model**: Uniform binary breakage is assumed, where a parent particle of diameter d fragments into two daughter particles of equal volume ($v/2$), corresponding to daughter diameters of $d/2^{1/3}$.
- **Conservation check**: At each time step, the total hydrate volume computed from the PBM ($\int \frac{\pi}{6} d^3 n(d, t)\, dd$) is monitored to ensure numerical conservation. The relative discrepancy in total particle volume between consecutive time steps is maintained below the solver tolerance.

Convergence and Conservation Verification

To ensure the numerical reliability of the PBM solution, systematic convergence tests were conducted using the 140 min Archimede loop condition as a representative case.

Grid convergence: The mean chord length was computed using 48, 64, and 80 logarithmically spaced size bins. The relative difference between the 64-bin and 80-bin solutions is 0.73%, which is below the 1% convergence threshold. The 64-bin grid is therefore adopted as the standard configuration, balancing accuracy and computational efficiency.

Time-step convergence: The time-step independence was verified using $\Delta t = 0.05$, 0.1, and 0.2 min. The relative difference in mean chord length between the 0.1 min and 0.05 min solutions is less than 0.01%, confirming that the adaptive time-stepping scheme with initial $\Delta t = 0.1$ min is sufficiently resolved.

Volume conservation: The total hydrate volume is defined as $V_{\mathrm{hyd}}(t) = \int \frac{\pi}{6} d^3 n(d,t)\, dd$, which accounts for all particles across the size domain. The maximum relative error in total hydrate volume over the entire simulation is 3×10^{-5} (0.003%), demonstrating that the numerical scheme preserves volume conservation to machine precision. This conservation holds across the nucleation source term, the volume-conserving aggregation kernel, and the breakage terms.

Model Parameter Classification

To clarify the independence of the model parameters, all input parameters are classified into two categories as summarized in Table 1: independently defined parameters (from literature or experimental conditions, not adjusted against FBRM validation data) and calibrated empirical coefficients (determined by fitting to experimental CLD data).

Table 1. Classification of model parameters.

Parameter	Value	Unit	Source/Method
Independently defined parameters			
Temperature T	277	K	Experimental condition [56]
Pressure P	7	MPa	Experimental condition [56]
Water fraction	0.30	–	Experimental condition [56]
Anti-agglomerant	0.005	wt/wt water	Experimental condition [56]
Pipe diameter (Lyre)	0.05	m	[56]
Pipe diameter (Archimede)	0.01	m	[56]
Reynolds number (Lyre)	35,000	–	[56]
Reynolds number (Archimede)	210	–	[56]
Shear rate (Lyre)	320	1/s	$\gamma = 8u/D_{\mathrm{pipe}}$
Shear rate (Archimede)	48	1/s	$\gamma = 8u/D_{\mathrm{pipe}}$
Oil phase density ρ_o	768	kg/m^3	Balakin/Fidel-Dufour (literature)
Oil phase viscosity μ_o	0.002194	Pa·s	Derived from Re and ρ_o
Primary particle size D_p	4 (Lyre), 7 (Archimede)	µm	[56]
Fractal dimension D_f	2.5–2.7	–	[56]
Calibrated empirical coefficients			
Combined interfacial parameter $\sigma \cos\theta$	Case-dependent	N/m	Calibrated against experimental CLD
Aggregation coefficient K_A	Case-dependent	–	Calibrated against experimental CLD
Breakage coefficient k_b	Case-dependent	1/m	Calibrated against experimental CLD
Initial PSD width $\sigma_{\log}$	Case-dependent	–	Calibrated against experimental CLD

The core physical framework of the model—including the Derjaguin capillary bridge force formulation, the volume-conserving PBM agglomeration term, and the population balance structure—is established independently of the validation data. The calibrated coefficients ($\sigma \cos\theta$, K_A, k_b, and $\sigma_{\log}$) are determined by fitting to the experimental CLD data; the remaining physical parameters are specified independently from the literature or experimental conditions.

4. Analysis of Simulation Results

4.1. Hydrate Particle Chord Length Distribution

This paper conducts a validation investigation based on the FBRM in situ measured chord length distribution data by Hung Leba [56]. The DCSMHyK-PBM model directly solves for the equivalent particle-size distribution (PSD) of hydrate particles. Relying on the geometric-probability model of random laser beam truncation by spherical particles, the predicted PSD is converted to chord length distribution (CLD) for direct comparison with FBRM experimental measurements. The validation covers six representative time points from two experimental flow loop systems: t = 97, 180, 240, and 320 min from the Lyre loop, and t = 140 and 170 min from the Archimede loop, under the operating conditions of T = 277 K, P = 7 MPa, 30% vol. water, and 0.5% additive (wt/wt water). Among these, t = 97, 140, 170, and 240 min are used as the calibration set for determining model parameters, while t = 180 and 320 min are reserved as an independent validation set not involved in parameter calibration.

As shown in Figures 7–10, the predicted CLD by DCSMHyK-PBM exhibits reasonable overall agreement with the experimental CLD across all four time points and both loop systems, successfully reproducing the key distribution characteristics of hydrate particle size under different flow regimes. In the small chord length segment (1–6 μm), the model prediction shows high consistency with the experimental data, accurately capturing the main peak position and the rising/falling characteristics of the CLD.

Figures 7 and 10 present the CLD comparison for the Lyre loop, which operates under turbulent flow conditions ($Re \approx$ 35,000, 5 cm inner diameter, shear rate $\gamma \approx 320\ s^{-1}$). At t = 97 min, the system is dominated by nascent hydrate fine particles with limited inter-particle agglomeration, and the experimental CLD exhibits a narrow unimodal distribution with the main peak located at approximately 2.4 μm (peak height 4.3%). The model demonstrates excellent predictive capability at this condition, accurately capturing the peak position (2.4 μm), distribution width, and overall shape of the experimental CLD. The predicted peak height (4.6%) is slightly higher than the experimental value, which can be attributed to the ideal spherical particle assumption. From t = 97 to 240 min within the Lyre loop, the experimental CLD broadens with an extended long tail towards large chord lengths, and the main peak shifts slightly from 2.4 to 2.8 μm, indicating enhanced agglomeration and the persistence of a fraction of large agglomerates. The model reasonably captures this distribution broadening and the long-tail feature, although the predicted main peak position (7.0 μm) is shifted to larger chord lengths compared with the experiment, suggesting that the model's agglomeration kernel may overestimate the degree of particle aggregation under the high-shear turbulent conditions at the later stage.

Figures 8 and 9 present the CLD comparison for the Archimede loop, which operates under laminar flow conditions ($Re \approx$ 210, 1 cm inner diameter, shear rate $\gamma \approx 48\ s^{-1}$). A notable feature of the experimental CLD in the Archimede loop is the bimodal distribution: a primary peak in the small-particle range (5–6 μm) coexists with a secondary peak in the large-agglomerate range (16–25 μm), reflecting the simultaneous presence of newly formed fine hydrate particles and multi-level agglomerates under the low-shear laminar conditions. At t = 140 min, the predicted CLD displays a broad distribution with the main peak near 10 μm and a shoulder emerging in the 14–15 μm range; the bimodal structure is less pronounced in the simulation compared with the experiment, which is attributed to the equivalent spherical particle assumption and the simplified agglomeration efficiency formula that tend to smooth out the discrete multi-level agglomerate structure. From t = 140 to 170 min within the Archimede loop, both the experimental and predicted CLD show broadening of the distribution width and enhanced multi-level agglomeration, consistent with the prolonged low-shear environment. At t = 170 min, the experimental CLD exhibits

a more pronounced multi-peak structure with peaks at approximately 5.4, 16, and 25 µm, while the model predicts a broad distribution with the main peak near 16 µm, reasonably capturing the large-agglomerate fraction although the fine-particle primary peak at 5.4 µm is less resolved.

Overall, the DCSMHyK-PBM model demonstrates reliable predictive capability for hydrate particle chord length distribution in both the turbulent Lyre loop and the laminar Archimede loop systems. The model accurately captures the main peak characteristics and distribution morphology across all four time points. A clear distinction between the two loop systems is observed: the turbulent Lyre loop (high shear rate, 320 s^{-1}) produces predominantly unimodal CLDs with small particle sizes, while the laminar Archimede loop (low shear rate, 48 s^{-1}) produces bimodal CLDs with significantly larger particle sizes, reflecting the stronger agglomeration environment under low-shear conditions. The model successfully resolves this flow-regime-dependent difference in CLD morphology. The observed discrepancies, including the peak position shift in the Lyre loop at $t = 240$ min and the less pronounced secondary peak in the Archimede loop, are primarily attributed to the equivalent spherical particle assumption and the simplified agglomeration efficiency formula, which represent common simplifications in population balance modeling.

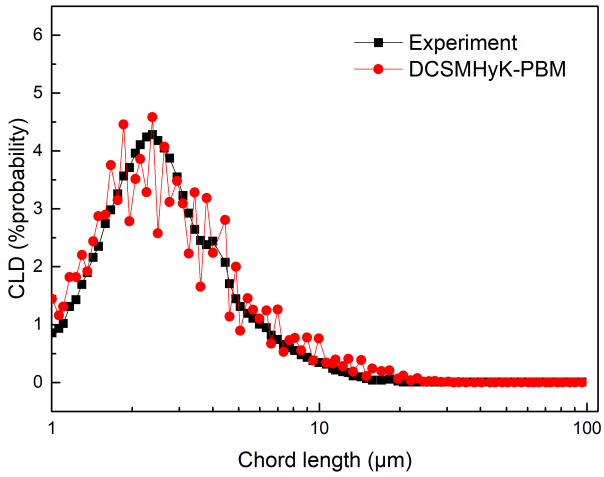


Figure 7. Hydrate particle chord length distribution ($t = 97$ min, $T = 277$ K, $P = 7$ MPa, 30% vol. water, 0.5% add).

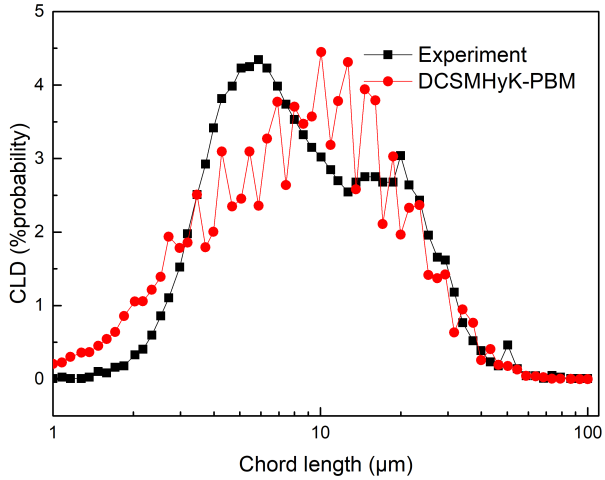


Figure 8. Hydrate particle chord length distribution ($t = 140$ min, $T = 277$ K, $P = 7$ MPa, 30% vol. water, 0.5% add).

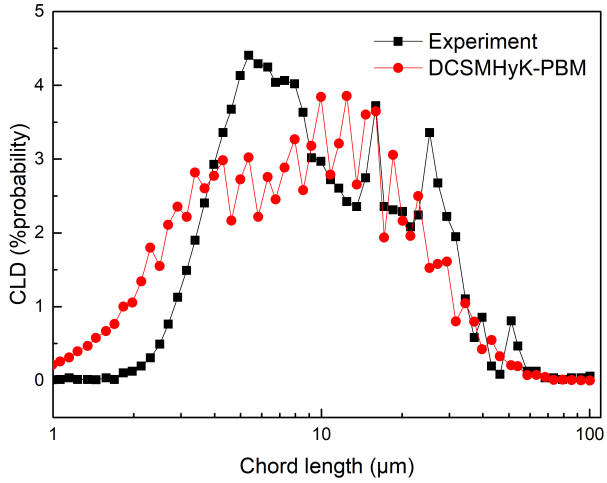


Figure 9. Hydrate particle chord length distribution (t = 170 min, T = 277 K, P = 7 MPa, 30% vol. water, 0.5% add).

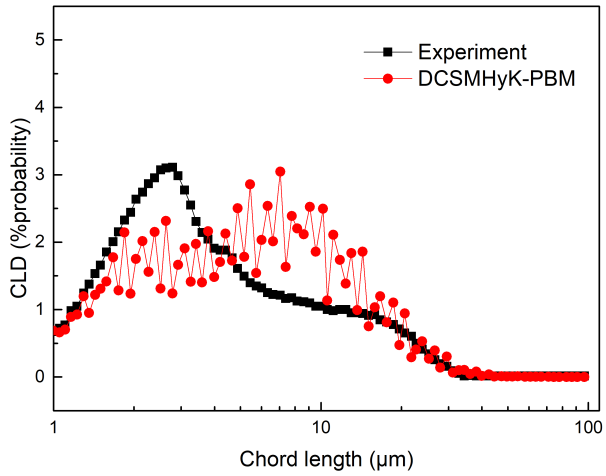


Figure 10. Hydrate particle chord length distribution (t = 240 min, T = 277 K, P = 7 MPa, 30% vol. water, 0.5% add).

Two additional time points (t = 180 and 320 min) were used as an independent validation set to assess the model performance outside the calibration data as shown in Figures 11 and 12. These observations were not involved in the determination of model parameters.

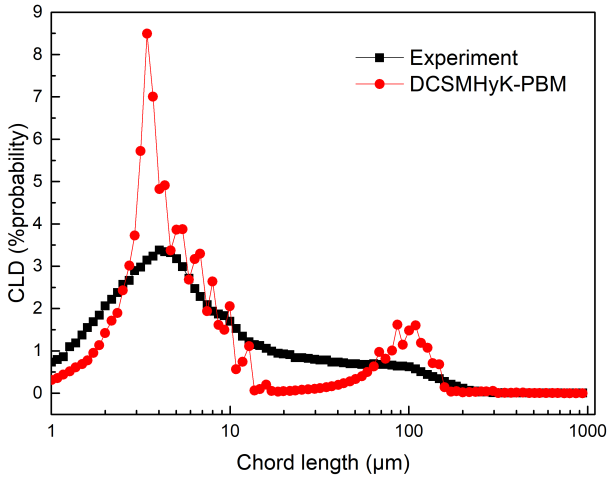


Figure 11. Hydrate particle chord length distribution (t = 180 min, independent validation set, T = 277 K, P = 7 MPa, 30% vol. water, 0.5% add).

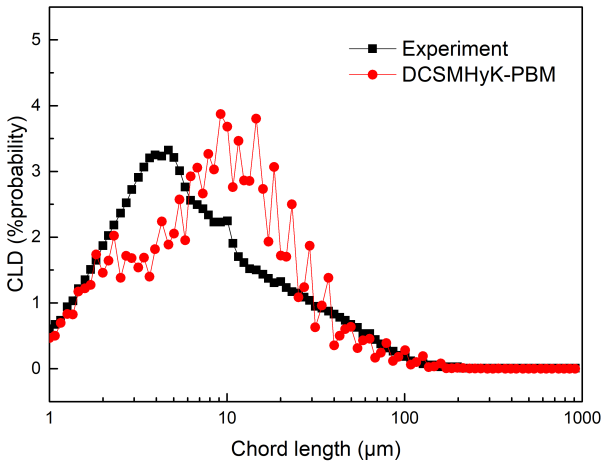


Figure 12. Hydrate particle chord length distribution (t = 320 min, independent validation set, T = 277 K, P = 7 MPa, 30% vol. water, 0.5% add).

At t = 180 min, the experimental CLD shows a unimodal distribution with the main peak near 5 μm and an extended tail toward large chord lengths up to 1000 μm, indicating the persistence of large agglomerates under prolonged turbulent flow. The model captures the main peak position and the overall distribution width, although the predicted peak height is somewhat elevated and a secondary feature appears around 100 μm. The average chord length is 17.83 μm experimentally and 19.25 μm from the simulation, corresponding to a relative error of 8.00%.

At t = 320 min, the experimental CLD remains unimodal with the primary peak near 5 μm. The simulated CLD exhibits a broader distribution with a secondary feature around 10 μm, while the primary peak position is reasonably reproduced. The average chord length is 13.06 μm experimentally and 13.30 μm from the simulation, with a relative error of 1.85%.

The mean absolute relative deviation over the two independent validation time points is 4.93%, suggesting that the model possesses a certain degree of generalizability beyond the calibration dataset.

4.2. Average Spheroid Chord Length of Hydrates

To further evaluate the prediction accuracy of the DCSMHyK-PBM model from a quantitative perspective, the theoretical mean chord lengths obtained from the model at six representative time points (four calibration and two independent validation) were compared with the experimentally measured mean chord lengths by FBRM. The average relative deviation (ARD) used in this study is defined as the mean absolute relative deviation (MARD):

$$\mathrm{ARD} = \frac{1}{N}\sum_{i=1}^{N}\left|\frac{d_{\mathrm{exp},i} - d_{\mathrm{sim},i}}{d_{\mathrm{exp},i}}\right| \times 100\%, \tag{26}$$

where N is the number of validation time points, and $d_{\mathrm{exp},i}$ and $d_{\mathrm{sim},i}$ are the experimental and simulated average chord lengths at the i-th time point, respectively. The results are shown in Figure 13 and Table 2.

The quantitative comparison of average chord lengths is summarized in Table 2. For the Lyre loop (turbulent conditions), the experimental average chord lengths are 3.18 μm at t = 97 min and 5.72 μm at t = 240 min, with corresponding simulated values of 3.40 and 6.86 μm. For the Archimede loop (laminar conditions), the experimental average chord lengths are 11.37 μm at t = 140 min and 12.76 μm at t = 170 min, with simulated values of 11.09 and 11.11 μm, respectively. The average chord lengths in the Archimede loop are significantly higher than those in the Lyre loop, consistent with the CLD analysis showing that the low-shear laminar conditions promote stronger particle agglomeration. The relative

errors for the four calibration time points are 6.87%, 2.47%, 12.96%, and 19.95%, respectively, with a calibration set MARD of 10.56%. For the two independent validation time points (t = 180 and 320 min), the relative errors are 8.00% and 1.85%, with a validation set MARD of 4.93%. The overall MARD across all six time points is 8.68%.

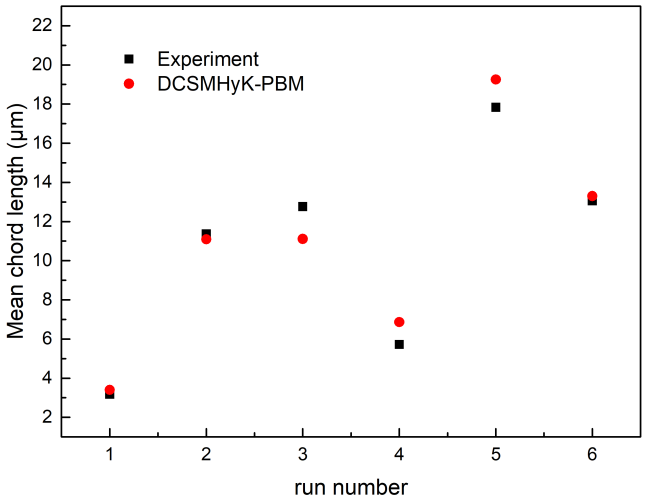


Figure 13. Comparison between experimental and simulated average chord lengths of hydrate particles.

Table 2. Comparison of experimental and simulated average chord lengths and relative errors of hydrate particles.

Time (min)	*Calibration Set*			*Independent Validation Set*		
	97	**140**	**170**	**240**	**180**	**320**
Experimental value/μm	3.18	11.37	12.76	5.72	17.83	13.06
Simulated value/μm	3.40	11.09	11.11	6.86	19.25	13.30
Relative Error	6.87%	2.47%	12.96%	19.95%	8.00%	1.85%
Calibration set MARD: 10.56%		Validation set MARD: 4.93%		Overall MARD: 8.68%		

For the Lyre loop conditions (turbulent flow, high shear rate), the model prediction accuracy varies between the calibration time points. At t = 97 min, the system is characterized by limited inter-particle agglomeration, and particle size is mainly controlled by hydrate formation kinetics rather than agglomeration dynamics. The model inherits the mature shell-growth kinetic equation of CSMHyK, resulting in good prediction accuracy with a relative error of 6.87%. At t = 240 min, the predicted average chord length (6.86 μm) is higher than the experimental value (5.72 μm), resulting in a relative error of 19.95%. This discrepancy may be attributed to the model's agglomeration kernel, which may overestimate the degree of particle aggregation under the high-shear turbulent conditions, or the breakage kernel, which may slightly underestimate the intensity of shear-induced fragmentation.

For the Archimede loop conditions (laminar flow, low shear rate), the average chord lengths are significantly higher (11.37 and 12.76 μm), reflecting the strong agglomeration environment in this loop system. At t = 140 min, the model achieves good prediction accuracy with a relative error of 2.47%, despite the secondary peak being less pronounced and shifted to smaller sizes. The accurate average chord length prediction suggests that the model reasonably balances the contributions of fine particles and large agglomerates in the size distribution. At t = 170 min, the predicted average chord length (11.11 μm)

is lower than the experimental value (12.76 μm), resulting in a relative error of 12.96%. This underestimation is consistent with the CLD analysis showing that the model's fine-particle primary peak is less resolved, although the large-agglomerate fraction is reasonably captured. The discrepancies in the Archimede loop are primarily attributed to the equivalent spherical particle assumption, which cannot fully characterize the irregular shape and complex pore structure of actual fractal agglomerates, and the simplified agglomeration efficiency formula, which tends to smooth out the discrete multi-level agglomerate structure into a continuous distribution.

The above analysis demonstrates that the DCSMHyK-PBM model achieves reliable prediction performance across both loop systems and all six time points, with an overall MARD of 8.68%. The calibration set MARD is 10.56%, while the independent validation set MARD is 4.93%, indicating that the model maintains reasonable predictive accuracy for time points outside the calibration dataset. Particularly noteworthy is the model's good accuracy at $t = 140$ min in the Archimede loop (2.47%) and $t = 320$ min in the validation set (1.85%), which validates the effectiveness of the inherited CSMHyK shell-growth kinetics and the Derjaguin capillary bridge adhesion mechanism. Furthermore, the model successfully resolves the bimodal distribution characteristic in the laminar Archimede loop and the flow-regime-dependent difference in CLD morphology between turbulent and laminar conditions, capabilities that steady-state equilibrium models cannot provide. By coupling the Derjaguin microscopic liquid bridge adhesion mechanism with the PBM dynamic evolution framework, the model captures the essential physics of hydrate particle agglomeration and provides quantitative predictions of average chord length. The remaining discrepancies are associated with well-known simplifications in population balance modeling, including the equivalent spherical assumption and simplified agglomeration efficiency, which represent common trade-offs between physical completeness and computational efficiency.

Combining the CLD morphological characteristics from Section 4.1, it can be observed that multi-level cluster formation is a common feature in both loop systems, and the model's ability to resolve this feature represents a key advantage over steady-state equilibrium models. The remaining discrepancies originate from the inherent complexity of the hydrate agglomeration process rather than a flaw in the core kinetic framework.

4.3. Model Limitations and Future Work

Several limitations of the current study should be acknowledged.

First, the model validation is based on six time points (four calibration and two independent validation) from two experimental flow loop systems (Lyre and Archimede) under a single set of bulk operating conditions ($T = 277$ K, $P = 7$ MPa, 30 vol% water, 0.5% anti-agglomerant). However, these two loop systems represent fundamentally different flow regimes: the Lyre loop operates under turbulent conditions ($Re \approx 35{,}000$) with a 5 cm inner diameter, while the Archimede loop operates under laminar conditions ($Re \approx 210$) with a 1 cm inner diameter. The 6.7-fold difference in shear rate and 5-fold difference in pipe diameter provide meaningful support for the model's applicability across different flow environments. Nevertheless, validation under a broader range of temperatures, pressures, and water contents would further establish the model's universality and will be pursued in future work as additional experimental datasets become available.

Second, the aggregation coefficient K_A and breakage rate coefficient k_b are calibrated against the experimental CLD data at each operating condition. Therefore, the present validation demonstrates the model's capability to reproduce the observed particle size distributions under the given conditions, rather than a fully independent prediction with fixed coefficients across all conditions. A fully predictive validation with fixed coefficients across multiple flow conditions will be addressed in future work.

Third, the model prediction accuracy decreases during the rapid hydrate formation stage and at high solid fractions, where the quasi-steady agglomeration assumption and the simplified breakage kernel become less applicable. Improving the model's performance in these transient stages represents an important direction for future work.

Fourth, the equivalent spherical particle assumption cannot fully characterize the irregular shape and complex pore structure of actual fractal agglomerates. Introducing a non-spherical particle shape factor and optimizing the agglomeration efficiency formula to account for fractal dimension effects will be pursued in future work.

5. Conclusions

This work proposes a DCSMHyK-PBM coupling model that addresses three key drawbacks of the conventional CSMHyK model: empirical adhesion-force treatment, inability to represent dynamic particle evolution, and generation of merely a single equilibrium particle size. The Derjaguin capillary liquid-bridge adhesion mechanism replaces the empirical subcooling-based cohesion formula, realizing physical closure of inter-particle cohesion through the combined interfacial parameter $\sigma \cos \theta$ and the effective particle radius. The population balance model (PBM) with time-dependent partial differential equations replaces the steady-state algebraic particle-size formula, enabling dynamic output of the full particle size distribution and average agglomerate size. The model maintains compatibility with industrial transient multiphase flow frameworks through a time-stepping iteration logic.

Validation against FBRM in situ measured chord length distribution data at six representative time points (four calibration and two independent validation) shows that the predicted CLD curves are consistent with experimental trends, reasonably capturing the main peak position and peak-shifting behavior. The overall mean absolute relative deviation (MARD) of the mean chord length is 8.68%, with a maximum relative error of 19.95%, demonstrating that the improved model provides reasonable dynamic prediction of hydrate particle size evolution.

The model deviations mainly stem from the ideal spherical particle assumption, constant kinetic parameters, and the simplification of microscopic processes, including hydrate ripening and wall deposition. Future work will focus on introducing a non-spherical particle shape factor, optimizing the agglomeration efficiency formula to account for fractal dimension effects, and further validating the model against a broader range of experimental data, including different water cuts, temperatures, pressures, and additive concentrations.

From the perspective of energy engineering, the proposed DCSMHyK-PBM model provides information on the evolution of hydrate agglomerate sizes, which can serve as one of the contributing factors in flow assurance risk assessment for deepwater oil-and-gas pipelines. The dynamic prediction of hydrate particle size evolution can support the design of proactive hydrate management strategies. It should be noted that particle size or average agglomerate size is not a direct quantitative measure of deposition rate, blockage probability, or time to pipeline blockage; a comprehensive flow assurance assessment requires integration with additional factors such as deposition kinetics, wall adhesion, and multiphase flow behavior. This work contributes to the broader effort toward safe, reliable, and efficient transportation of natural gas in offshore energy production systems.

Author Contributions: Conceptualization, J.H.; methodology, J.H.; software, J.H.; validation, J.H.; formal analysis, J.H.; investigation, J.H.; resources, X.S.; data curation, J.H.; writing—original draft preparation, J.H.; writing—review and editing, X.S., K.Z. and S.J.; visualization, J.H.; supervision, X.S.; project administration, X.S. All authors have read and agreed to the published version of the manuscript.

Funding: This research received no external funding.

Institutional Review Board Statement: Not applicable.

Informed Consent Statement: Not applicable.

Data Availability Statement: The data presented in this study are available within the article.

Acknowledgments: The authors would like to thank Hung Leba and co-workers for providing the FBRM experimental data used for model validation in this work.

Conflicts of Interest: The authors declare no conflicts of interest.

Abbreviations

The following abbreviations are used in this manuscript:

CSMHyK	Colorado School of Mines Hydrate Kinetics model
DCSMHyK	Derjaguin-corrected CSMHyK model
PBM	Population Balance Model
PBE	Population Balance Equation
FBRM	Focused Beam Reflectance Measurement
CLD	Chord Length Distribution
PSD	Particle Size Distribution
CFD	Computational Fluid Dynamics
ARD	Average Relative Deviation

Nomenclature

Symbol	Description	Unit
μ_r	Relative viscosity of the suspension	–
μ_a	Apparent viscosity of the suspension	Pa·s
μ_o	Viscosity of the oil phase	Pa·s
ϕ_e	Effective volume fraction of hydrate agglomerates	–
ϕ_{hyd}	Volume fraction of hydrate particles	–
$\phi_{\max}$	Maximum packing volume fraction	–
d_a	Average diameter of hydrate agglomerate particles	µm
d_0	Diameter of initial hydrate particles	µm
f	Fractal dimension of hydrate agglomerate particles	–
d	Water droplet diameter	m
We	Weber number	–
ρ_o	Oil phase density	kg/m^3
u	Average flow velocity/axial velocity of slurry	m/s
θ	Contact angle (component of combined parameter)	°
σ	Interfacial tension (component of combined parameter)	N/m
Re	Reynolds number	–
$d_{a,\max}$	Maximum size of hydrate agglomerate particles	µm
F_a	Cohesive/adhesion force between hydrate particles	N
γ	Shear rate	1/s
ΔT	System subcooling relative to hydrate equilibrium	K
H	Separation distance between two particles	m
k	Interaction coefficient between particles	–
R	Effective radius of two contacting hydrate particles ($R_{\text{eff}} = R_1R_2/(R_1 + R_2)$)	m
R_1, R_2	Radii of two contacting hydrate particles	m
U	Interaction energy per unit area between particles	J/m^2
θ	Contact angle between hydrate and liquid phases	°
$n(d,t)$	Number density of hydrate particles of size d at time t	1/m^4
x	Axial position of the pipe	m
B_a	Agglomeration birth (source) term	1/m^4/s
D_a	Agglomeration death (sink) term	1/m^4/s
B_b	Breakage birth (source) term	1/m^4/s

D_b	Breakage death (sink) term	$1/m^4/s$
α_a	Agglomeration efficiency	–
F_s	Shear force exerted by fluid on particles	N
$\beta(d_i, d_j)$	Collision frequency between two particles	1/s
d_i, d_j	Diameters of two colliding hydrate particles	m
$S(d)$	Dissociation (breakage) rate of hydrate agglomerates	1/s
k_b	Breakage rate coefficient	1/m
$b(d\|d')$	Probability distribution of daughter particles	1/m
$d_A(t)$	Average agglomerate size at time t	µm
n_0	Initial number concentration of primary hydrate particles	$1/m^3$
d_p	Hydrate particle diameter	m
Δt	Time step	s
B_{nuc}	Hydrate nucleation/growth source term	$1/m^4/s$
$\dot{N}_{new}$	Number generation rate of primary hydrate particles	$1/m^3/s$
$\delta(\cdot)$	Dirac delta function	1/m

References

1. Olajire, A.A. Flow assurance issues in deep-water gas well testing and mitigation strategies with respect to gas hydrates deposition in flowlines—A review. *J. Mol. Liq.* **2020**, *318*, 114015. [CrossRef]
2. Umuteme, O.M.; Islam, S.Z.; Hossain, M.K.A. Analytical modelling of the hydraulic effect of hydrate deposition on transportability and plugging location in subsea gas flowlines. *Proc. Inst. Mech. Eng. Part C J. Mech. Eng. Sci.* **2024**, *238*, 4812–4830. [CrossRef]
3. Katoh, A.; Nakayama, K.; Baba, K. Model simulation for generation and migration of methane hydrate. *Energy Explor. Exploit.* **2000**, *18*, 401–421. [CrossRef]
4. Miguel, J.; Torrejón, C.; Romero-Guzmán, C.; Piñeiro, M.M.; Blas, F.J.; Algaba, J. Simulation of the THF hydrate–water interfacial free energy from computer simulation. *J. Chem. Phys.* **2024**, *161*, 114703. [CrossRef] [PubMed]
5. Wang, Y.; Subramanian, S.; Estanga, D.; Majid, A.A.A.; Hu, S.; Salmin, D.C.; Koh, C.A.; Zerpa, L.E. Changing the Hydrate Management Guidelines: From Benchtop Experiments to CSMHyK Field Simulations. *Energy Fuels* **2020**, *34*, 13523–13535. [CrossRef]
6. Wang, Y.; Koh, C.A.; Dapena, J.A.; Zerpa, L.E. A transient simulation model to predict hydrate formation rate in both oil- and water-dominated systems in flowlines. *J. Nat. Gas. Sci. Eng.* **2018**, *59*, 9–21.
7. Mandal, A.; Laik, S. Modeling of Gas Hydrate Formation in a High Pressure Reactor. *Int. J. Chem. React. Eng.* **2008**, *6*, A17. [CrossRef]
8. Balkin, B.V.; Hoffmann, A.C.; Kosinski, P.; Rhyne, L.D. Eulerian-Eulerian Simulation of Sedimentation of Uniformly-sized, non-Brownian Spheres in Viscous Fluids. *AIP Conf. Proc.* **2008**, *1048*, 272–275. [CrossRef]
9. Hashemi, S.; Macchi, A. Gas Hydrate Growth Model in a Semibatch Stirred Tank Reactor. *Ind. Eng. Chem. Res.* **2007**, *46*, 5907–5912. [CrossRef]
10. Sloan, E.D. A changing hydrate paradigm—From apprehension to avoidance to risk management. *Fluid Phase Equilib.* **2005**, *228–229*, 67–74. [CrossRef]
11. Camargo, R.; Palermo, T. Rheological properties of hydrate suspensions in an asphaltenic crude oil. In Proceedings of the 4th International Conference of Gas Hydrates, Yokohama, Japan, 19–23 May 2002; pp. 880–885.
12. Charlton, T.B.; Norris, B.W.E.; Johns, M.L.; May, E.F.; Aman, Z.M.; Zerpa, L.E. Predicting hydrate film growth on the wall from water droplet deposition in gas-dominated flowlines. In Proceedings of the 19th International Conference on Multiphase Production Technology (MPT 2019), Cannes, France, 5–7 June 2019.
13. Zerpa, L.E.; Sloan, E.D.; Sum, A.K.; Koh, C.A. Overview of CSMHyK: A transient hydrate formation model. *J. Pet. Sci. Eng.* **2012**, *98–99*, 122–129. [CrossRef]
14. Zerpa, L.E. A Practical Model to Predict Gas Hydrate Formation, Dissociation and Transportability in Oil and Gas Flowlines. Ph.D. Thesis, Colorado School of Mines, Golden, CO, USA, 2013.
15. Geranutti, B.L.S.; Pohl, M.; Rathmaier, D.; Karimi, S.; Prasad, M.; Zerpa, L.E. Multiphysics Measurements for Detection of Gas Hydrate Formation in Undersaturated Oil Coreflooding Experiments with Seawater Injection. *Energies* **2024**, *17*, 3280. [CrossRef]
16. Srivastava, V.; Majid, A.A.A.; Warrier, P.; Grasso, G.; Koh, C.A.; Zerpa, L.E. Hydrate-Bedding Mechanisms in Partially Dispersed Water/Oil Systems. *SPE J.* **2019**, *25*, 925–937. [CrossRef]
17. Boxall, J.; Davies, S.; Koh, C.A.; Sloan, E.D.; Sum, A.K.; Dieker, L.E.; Aman, Z.M. Predicting where and when hydrate plugs form in oil-dominated flowlines. *SPE Proj. Facil. Constr.* **2009**, *4*, 80–86. [CrossRef]
18. Boxall, J. Hydrate Plug Formation from 50% Water Content Water-in-Oil Emulsions. Ph.D. Thesis, Colorado School of Mines, Golden, CO, USA, 2009.
19. Boxall, J.A.; Koh, C.A.; Sloan, E.D.; Sum, A.K.; Wu, D.T. Droplet size scaling of water-in-oil emulsions under turbulent flow. *Langmuir* **2012**, *28*, 104–110. [CrossRef] [PubMed]

20. Sinquin, A.; Palermo, T.; Peysson, Y. Rheological and flow properties of gas hydrate suspensions. *Oil Gas. Sci. Technol.* **2004**, *59*, 41–57. [CrossRef]
21. Charlton, T.B.; Di Lorenzo, M.; Zerpa, L.E.; Koh, C.A.; Johns, M.L.; May, E.F.; Aman, Z.M. Simulating Hydrate Growth and Transport Behaviour in Gas-dominated Flow. *Energy Fuels* **2017**, *31*, 11210–11220. [CrossRef]
22. Kannan, S.N.; Torsvik, M.; Ugueto, L.; Hatscher, S.; Ravichandran, S.; Sloan, D.; Zerpa, L.E.; Koh, C. Safe and Successful Gas Hydrate Plug Remediation in Vega Asset—Norwegian Gas Condensate Subsea Production System. In Proceedings of the SPE Annual Technical Conference and Exhibition, San Antonio, TX, USA, 16–18 October 2023.
23. Balakin, B.V.; Hoffmann, A.C.; Kosinski, P. Population balance model for nucleation, growth, agglomeration, and breakage of hydrate particles in turbulent flow . *AIChE J.* **2010**, *56*, 2041–2054. [CrossRef]
24. Gal, P.L.; Snoussi, W.; Rondon, M.; Laffray, G.; Laudet, J.-B.; Palermo, T. Optimizing Subsea Processing for Deep and Long Step-Out Gas Fields. In Proceedings of the Offshore Technology Conference (OTC), Houston, TX, USA, 1–4 May 2023.
25. Balakin, B.V.; Hoffmann, A.C.; Kosinski, P.; Istomin, V.A.; Chuvilin, E.M.; Simos, T.E.; Psihoyios, G.; Tsitouras, C. Combined CFD/Population Balance Model for Gas Hydrate Particle Size Prediction in Turbulent flowline Flow. In Proceedings of the International Conference on Numerical Analysis and Applied Mathematics, Kos, Greece, 19–23 September 2010.
26. Yao, H.; Ding, L.; Guo, E.; Xie, Z.; Wang, Y.; Song, S.; Shi, B.; Gong, J. Hydrate Antiagglomerants Performance by Characterizing Particle Size Distribution In Situ Flow Condition. *Energy Fuels* **2024**, *38*, 16079–16088. [CrossRef]
27. Balakin, B.V.; Kartushinsky, A.A.; Hoffmann, A.C.; Kosinski, P. CFD-PBM modelling of agglomeration and deposition in petroleum industry. In Proceedings of the 11th International Conference on Multiphase Flow (ICMF), Tuscaloosa, AL, USA, 22–27 May 2016.
28. Yu, C.; Han, C.J.; Wang, L.; Jing, J.Q.; Li, Y.X.; Wang, W.C.; Song, X.C. Investigation of the Behavior of Hydrate Slurry Flow in the Bend Based on the CFD-PBM Approach. *Fluid Dyn.* **2023**, *58*, 684–700. [CrossRef]
29. Balakin, B.V.; Lo, S.; Kosinski, P.; Hoffmann, A.C. Modelling agglomeration and deposition of gas hydrates in industrial flowlines with combined CFD-PBM technique. *Chem. Eng. Sci.* **2016**, *155*, 45–57. [CrossRef]
30. Wang, S.; Mu, L.; Wang, C.; Li, X.; Xie, J.; Shang, Y.; Pu, H.; Dong, M. Modeling and Simulation of Micron Particle Agglomeration in a Turbulent Flow: Impact of Cylindrical Disturbance and Particle Properties. *ACS Omega* **2024**, *9*, 49302–49315. [CrossRef] [PubMed]
31. Liu, L.; Shi, W.; Li, B.; Wang, G.; Guo, Y.; Yang, X.; Zhou, W. CFD-PBM modelling for predicting the size and distribution of silica nanoparticles synthesized in an ultrasound-assisted swirling vortex flow reactor. *Ultrason. Sonochem.* **2025**, *123*, 107663. [CrossRef] [PubMed]
32. Zhao, Z.; Zuo, Z.; Qian, Z. Trapping and leakage of heavy inertial particles in an unequal strength counter-rotating vortex pair. *J. Fluid Mech.* **2025**, *1024*, A10. [CrossRef]
33. Liu, Z.; Li, Y.; Wang, W.; Song, G.; Ning, Y.; Liu, X.; Zhang, J. Investigation into the formation, blockage and dissociation of cyclopentane hydrate in a visual flow loop. *Fuel* **2022**, *307*, 121730. [CrossRef]
34. Struchalin, P.G.; Ye, V.H.; Kosinski, P.; Kosinski, P.; Hoffmann, A.C.; Balakin, B.V. Flow loop study of a cold and cohesive slurry, Pressure drop and formation of plugs. *Fuel* **2023**, *332*, 126061. [CrossRef]
35. Tan, H.; Li, J.; Chen, Z.; Ren, Q.; Wang, X.; Wang, J.; Yang, C.; Wang, Z. Numerical investigation of reactive crystallization of calcium sulfate dihydrate in the stirred reactor with a coupled CFD-PBM-CRM model. *Chem. Eng. Sci.* **2025**, *317*, 121708. [CrossRef]
36. Liu, W.; Wei, H.; Black, S. An Investigation of the Transformation of Carbamazepine from Anhydrate to Hydrate Using in Situ FBRM and PVM. *Org. Process Res. Dev.* **2009**, *13*, 494–500. [CrossRef]
37. Zhang, R.; Zhang, Y.; Chai, S.; Takyi, S.A.; Lin, Z.; Wang, X.; Xin, Y.; Li, E.; Zeng, F.; Panahov, G. The synergistic mechanism of CO_2 hydrate formation and blockage in flow loop system: Using a new FBRM experimental setup investigation. *Results Eng.* **2026**, *29*, 109027. [CrossRef]
38. Herri, J.M.; Leba, H.; Cameirao, A.; Darbouret, M.; Peytavy, J.L.; Glénat, P. Interpretation and modeling of chord length distribution from FBRM results during gas hydrate formation and agglomeration from water-in-oil emulsion. *Abstr. Pap. Am. Chem. Soc.* **2009**, *237*.
39. Song, Y.; Chen, C.; Hu, W. Gas hydrate nucleation and growth. In *Understanding Geologic Carbon Sequestration and Gas Hydrate from Molecular Simulation*; Elsevier: Amsterdam, The Netherlands , 2024; pp. 309–421.
40. Boxall, J.; Greaves, D.; Mulligan, J.; Koh, C.A. Gas hydrate formation and dissociation from water-in-oil emulsions studied using PVM and FBRM particle size analysis. In Proceedings of the 6th International Conference on Gas Hydrates (ICGH), Vancouver, BC, Canada, 6–10 July 2008.
41. Meindinyo, R.E.T.; Svartaas, T.M.; Nordb, T.N.; Bøe, R. Gas Hydrate Growth Estimation Based on Heat Transfer. *Energy Fuels* **2015**, *29*, 1501–1509. [CrossRef]
42. Ba, H.L.; Cameirão, A.; Herri, J.M.; Darbouret, M.; Peytavy, J.L.; Glénat, P. The use of FBRM probe during hydrate particles agglomeration. In Proceedings of the Société Française de Génie Des Procédés (SFGP), Marseille, France, 14–16 October 2009.

43. Bai, C.; Su, P.; Zhang, Y.; Xu, X.; Han, S. Mechanism whereby Sediment Properties Control Gas Hydrate Accumulation in Fine-Grained Sediments. *Energy Fuels* **2025**, *39*, 14198–14212. [CrossRef]
44. Liu, J.; Dong, T.; Lin, D.; Liang, D. Hydraulic Thermal Chemical Coupling Model Considering Hydrate Growth and agglomeration to Study the Hydrate Slurry Multiphase Flow in Oil–Water Systems. *Energy Fuels* **2024**, *38*, 10123–10133. [CrossRef]
45. Lv, X.; Ni, X.Y.; Zhao, Y.; Liu, T.; Jing, S.; Bai, B.; Liang, S.; Liu, Y.; Ma, Q.; Wang, C.; et al. Characterization of Carbon Dioxide Hydrate Growth Kinetics in Carbon Micron Tube Oil–Water System. *J. Energy Resour. Technol.* **2024**, *146*, 012903. [CrossRef]
46. Mi, F.; He, Z.; Ning, F. Molecular dynamics simulation on CO_2 hydrate growth and CH_4-CO_2 replacement in various clay nanopores. *Energy* **2025**, *314*, 133456. [CrossRef]
47. Ravesh, R.; Ansari, A.A.; Panigrahi, P.K.; Das, M.K. Hydrate growth at the guest-water interface in the presence of surfactant on the cyclopentane droplet. *Mater. Today Proc.* **2024**, *115*, 102764. [CrossRef]
48. Wang, W.; Xiao, Y.; Xu, Y.; Han, H.; Li, Y. Characteristics and mechanical properties of hydrate growth and deposition on the pipe walls in flow systems. *Fuel* **2025**, *389*, 138562. [CrossRef]
49. Kanani, P.; Ganesh, R.K.; Adil, M.; Metya, A.K. Impact of antifreeze and promoter on clathrate hydrate nucleation and growth. *J. Mol. Liq.* **2025**, *424*, 125987. [CrossRef]
50. Huang, X.; Zhu, Y.J.; Zhang, T.H.; Wang, G.-H.; Xiao, P.; Wang, X.-H.; Sun, C.-Y.; Chen, G.-J. Methane Hydrate Blockage in Gas–Water–Sand Systems: Insights from FBRM and PVM Analysis. *Energy Fuels* **2024**, *38*, 13567–13578. [CrossRef]
51. Zhang, A.Y.; Cai, M.; Wei, N.; Li, H.-T.; Zhang, C.; Pei, J.; Wang, X.-W. Analysis of sensitivity to hydrate blockage risk in natural gas gathering flowline. *Pet. Sci.* **2024**, *21*, 1567–1582. [CrossRef]
52. Hoffmann, A.C.; Finkers, H.J. A relation for the void fraction of randomly packed particle beds. *Powder Technol.* **1995**, *82*, 197–203. [CrossRef]
53. Muhle, K. Flock stability in laminar and turbulent flow. In *Coagulation and Flocculation: Theory and Applications; Chapter 8*; Marcel Dekker: New York, NY, USA, 1996.
54. Derjaguin, B.V. Untersuchungen über die Reibung und Adhäsion, IV. *Colloid Polym. Sci.* **1934**, *69*, 155–164. [CrossRef]
55. Rabinovich, Y.I.; Esayanur, M.S.; Moudgil, B.M. Capillary Forces between Two Spheres with a Fixed Volume Liquid Bridge: Theory and Experiment. *Langmuir* **2005**, *21*, 10992–10997. [CrossRef] [PubMed]
56. Hung Leba, H.; Cameirao, A.; Herri, J.M.; Darbouret, M.; Peytavy, J.-L.; Glénat, P. Chord length distributions measurements during crystallization and agglomeration of gas hydrate in a water-in-oil emulsion: Simulation and experimentation . *Chem. Eng. Sci.* **2010**, *65*, 1185–1200. [CrossRef]

Disclaimer/Publisher's Note: The statements, opinions and data contained in all publications are solely those of the individual author(s) and contributor(s) and not of MDPI and/or the editor(s). MDPI and/or the editor(s) disclaim responsibility for any injury to people or property resulting from any ideas, methods, instructions or products referred to in the content.